

Investigation of the Neighborhood Properties of Several Monatomic Liquids

Daniel J. Graham* and Bart Pilarski

Department of Chemistry, Loyola University of Chicago, Chicago, Illinois 60626

Received: June 23, 1999; In Final Form: October 26, 1999

The neighborhood properties of several monatomic liquids are investigated. This builds upon indirect methods (numerical techniques) explored in experiments with 2D foams (Graham et al., *J. Phys. Chem. B* **1997**, 101, 11211). In the foundation study, the methods were applied to the radial distribution function $G(r)$ for foams and liquid sodium. Further development is presented here so as to widen the method applicability and to learn more about neighborhood distributions. The method is demonstrated using $G(r)$ for hard spheres; favorable comparisons are found between the distributions so obtained and via the theory of Mazur (*J. Chem. Phys.* **1992**, 97, 9276). Using published $G(r)$ data, application is made to a diverse set of monatomics: lithium, potassium, argon, indium, gallium, and mercury. Overall, this research offers structure comparisons among different liquids and identifies neighborhood trends. In addition, a simple way to partition $G(r)$ is further established which requires no specification of the interaction potentials.

I. Introduction

For a fluid, the radial distribution function $G(r)$ describes the structure near a reference atom.¹ Yet how $G(r)$ is divided into sets of neighborhoods is never indicated in the data of origin. Theory and simulations have tackled this problem from several vantage points.^{2–6} Most recently, Keyes has related the neighborhood distributions of a Lennard-Jones fluid to the dynamics of glass formation.⁷

This paper revisits indirect methods explored in 2D foam studies.⁸ For that project, applications were made to $G(r)$ measured for 2D samples and analogous data published for liquid sodium. Here further development is presented so as to widen the method applicability and to learn more about liquid structure. To provide another benchmark, the method is demonstrated using $G(r)$ for hard spheres. Favorable comparisons are found between the neighborhood distributions so obtained, and those calculated via the theory of Mazur.⁶ Using published $G(r)$ data, applications are made to several materials: lithium, potassium, argon, indium, gallium, and mercury. These were chosen for their diversity and established structure data. The information in Table 1 attests to this diversity regarding atomic size, binding strength, and crystal structure.

This paper is organized as follows. Section II revisits the indirect methods and demonstrates their efficacy on hard sphere (HS) systems. In addition, several quantities are introduced which foster comparisons among different materials. Section III presents applications to six different liquids with the resulting trends and significance discussed in section IV.

Our purpose is 3-fold: (1) to illustrate properties of the neighborhood distributions for monatomic liquids, (2) to offer structure comparisons among a diverse set of materials, and (3) to further establish an indirect method as a simple way to partition $G(r)$. We were drawn to this topic during studies of

TABLE 1: Selected Elements and the Density, Melting Point, Boiling Point, and Structure of the Most Prevalent Crystalline Form^{11,12}

element	density	mp	bp	structure
Li	76.4 mol/L	459 K	1620 K	bcc
K	22.0 mol/L	335 K	1047 K	bcc
In	63.7 mol/L	428 K	2353 K	tetragonal
Ar	44.6 mol/L	84 K	87 K	fcc
Hg	67.8 mol/L	234 K	630 K	rhombohedral
Ga	84.8 mol/L	303 K	2676 K	orthorhombic (V _h Bmab)

both foams and crystallization resistance.⁹ Many results in the latter area did not appear understandable via time-honored chemical structure theory and X-ray diffraction. We thus sought an approach to liquid structure which could prove useful when knowledge of the interaction potentials was sketchy at best. This paper continues our efforts to learn about fluids via alternative experiments and analysis.¹⁰

II. $G(r)$, Neighborhood Distribution Functions and an Indirect Method for Partitioning

For fluids and crystals alike, $G(r)$ stems from diffraction data such as X-ray.¹ It is equivalent to a sum of individual functions:

$$G(r) = P_1(r) + P_2(r) + \cdots P_n(r) + \cdots + P_{N-1}(r) = \sum_{n=1}^{n=N-1} \quad (1)$$

where N is the total number of atoms and $P_n(r)$ describes the distribution of the n th nearest neighbor at radial distance r . It is unfortunate that unlike for a crystal, $G(r)$ for a fluid (liquid or interacting gas) lends scant insight into any of the right hand side terms. Further digging requires theory and modeling such as Monte Carlo and molecular dynamics (MC, MD).^{2–7} These begin by approximating the potentials operating between atoms.

* To whom correspondence should be addressed. Fax: (773) 508-3086; E-mail: dgraham@luc.edu

An alternative was explored in our work with foams.⁸ Such an “indirect method” sidestepped the potential specifics and educed from $G(r)$ neighborhood distributions in agreement with experiment. The method applicability can be widened here by first noting that in the ideal gas limit, $P_1(r)$ of eq 1 is given by

$$P_1(r) = G(r) \exp[-\int_0^r dr' G(r')] \quad (2)$$

A recursion relation then prescribes ideal gas $P_n(r)$ for all $n > 1$:

$$P_n(r) = \{G(r) - \sum_{m=1}^{n-1} P_m(r)\} \exp[-\int_0^r dr' \{G(r') - \sum_{m=1}^{n-1} P_m(r')\}] \quad (3)$$

As discussed previously, the indirect method allies a parameter λ_n with each distribution function and modifies eqs 1–3 accordingly:

$$G(r, \{\lambda_n\}) = P_1(r, \lambda_1) + P_2(r, \lambda_2) + \cdots P_n(r, \lambda_n) + \cdots + P_{N-1}(r, \lambda_{N-1})$$

$$= \sum_{n=1}^{N-1} P_n(r, \lambda_n) \quad (4)$$

$$P_1(r, \lambda_1) = a_1 G(r) \exp[-\lambda_1 \int_0^r dr' G(r')] \quad (5)$$

$$P_n(r) = \{G(r) - \sum_{m=1}^{n-1} P_m(r, \lambda_m)\} \times \exp[-\lambda_n \int_0^r dr' \{G(r') - \sum_{m=1}^{n-1} P_m(r', \lambda_m)\}] \quad (6)$$

The a_n are normalization coefficients dependent on the λ_n . In establishing “best-fit” $P_n(r, \lambda_n)$, five ideas come into play. First, eqs 5 and 6 offer the respective forms of $P_1(r, \lambda_1)$ and $P_n(r, \lambda_n)$, $n > 1$. Second and third, normalization

$$\int_0^\infty dr P_n(r, \lambda_n) = 1 \quad (7)$$

and the fact that each $P_n(r, \lambda_n)$ is positive definite impose strict boundaries on the allowable λ_n space. Fourth, since

$$(\partial G / \partial r)_{r=r_1} = (\partial \{G - P_1(r, \lambda_1)\} / \partial r)_{r=r_1} \quad (8)$$

where r_1 is the point at which $P_1(r, \lambda_1)$ demonstrates its maximum value, it follows that

$$\lambda_1 = \frac{(\partial G(r) / \partial r)_{r=r_1}}{G(r_1)^2} \quad (9)$$

Equations 8 and 9 owe to eq 5 and the fact that

$$(\partial P_1(r, \lambda_1) / \partial r)_{r=r_1} = 0 \quad (10)$$

It can similarly be shown that for $n > 1$

$$\lambda_n = \frac{(\partial \{G(r) - \sum_{m=1}^{n-1} P_m(r, \lambda_m)\} / \partial r)_{r=r_m}}{\{G(r_n) - \sum_{m=1}^{n-1} P_m(r_n, \lambda_m) G(r_n)\}^2} \quad (11)$$

where the summations extend from $m = 1$ to $m = n - 1$.

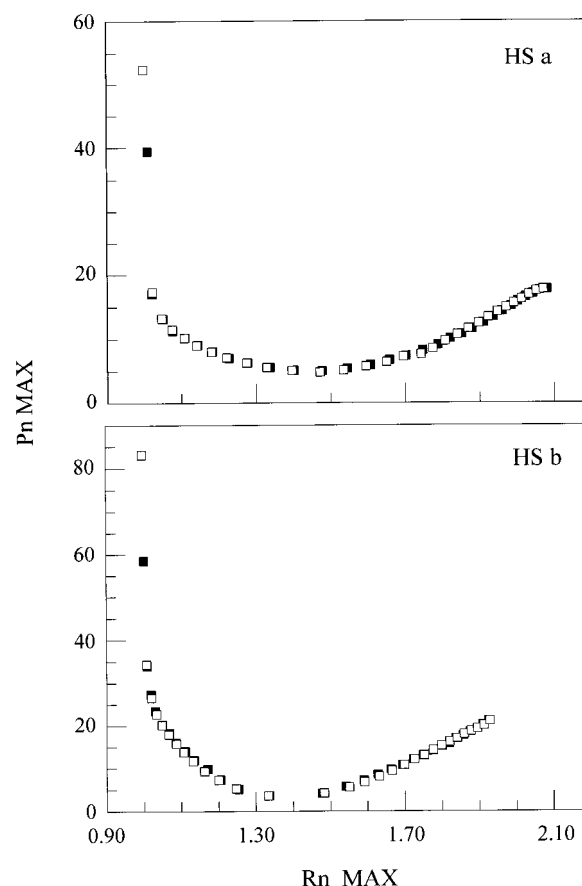


Figure 1. Maximum values of hard sphere neighborhood distributions as a function of r_n . Results from application of section II techniques (□) and the theory of Mazur (■).⁶ HS systems “a” and “b” refer to volume fractions of 0.419 and 0.524, respectively.

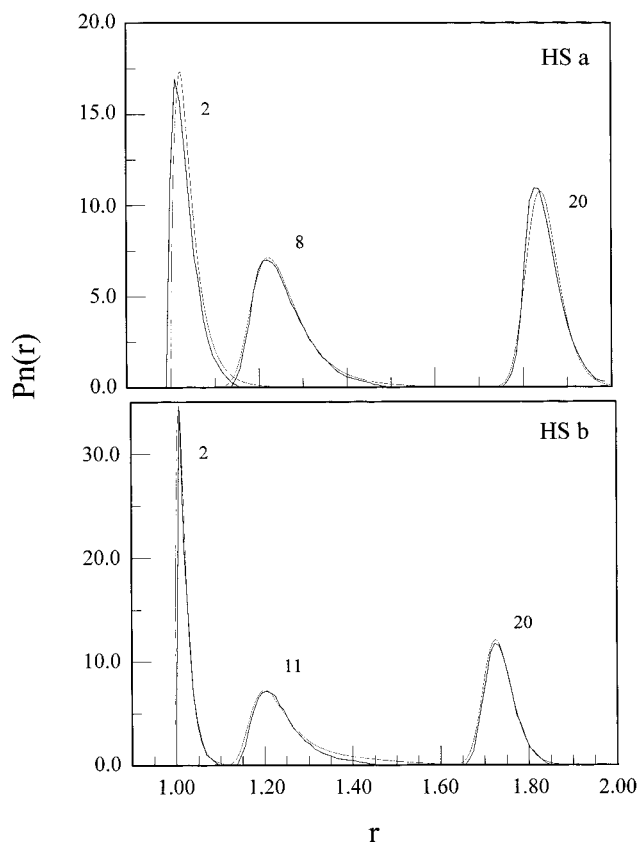


Figure 2. Several $P_n(r)$ for HS systems. Results of section II techniques (thinner lines) and theory. Data pertain to HS systems of Figure 1.

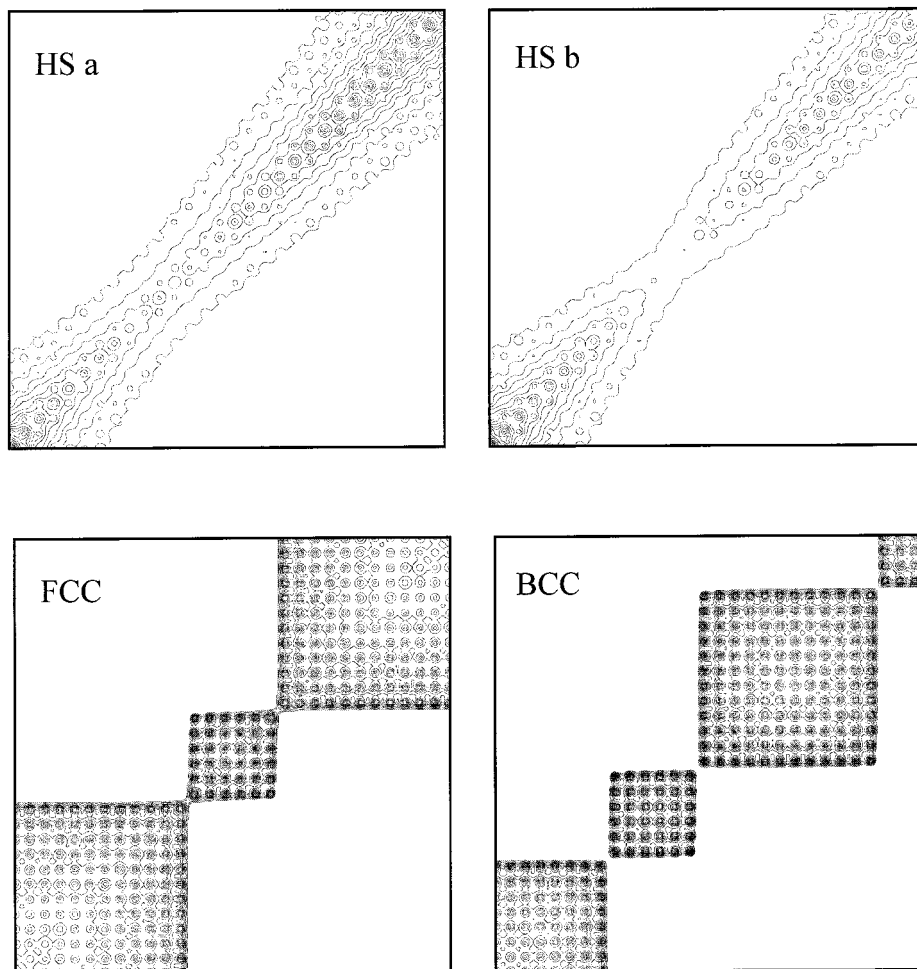


Figure 3. Contour plots derived from neighborhood overlap; $n, n' = 1-30$. Contour density is based on the section II techniques and eq 14 applied to the HS systems of Figure 1. Identical scaling parameters have been used in both cases; plots have been constructed using PSI-Plot (Poly Software International). The lower two panels show the neighborhood overlap for FCC and BCC crystals. The volume fractions for these systems are 0.740 and 0.680, respectively.

The fifth idea concerns the distribution maxima. From modeling work, we have found that r_1 is allied with the first local minimum of $(\partial^2 G(r)/\partial r^2)$. One thus obtains $P_1(r, \lambda_1)$ by examining the second derivatives of $G(r)$ and computed values of the right hand side of eq 9 and identifying the λ_1, r_1 which enable the normalization, positive-definite, and local minimum conditions to be met.

An expression for $P_2(r, \lambda_2)$ follows from eq 6. Since

$$(\partial G/\partial r)_{r=r_2} - (\partial\{G - P_2(r, \lambda_2)\}/\partial r)_{r=r_2} = 0 \quad (12a)$$

$$(\partial\{G - P_1(r, \lambda_1)\}/\partial r)_{r=r_2} - (\partial\{G - P_1(r, \lambda_1) - P_2(r, \lambda_2)\}/\partial r)_{r=r_2} = 0 \quad (12b)$$

$r_2 \geq r_1$ and λ_2 are established via eqs 6 and 11 and by minimizing the sum of squares eq 12. The best-fit $P_2(r, \lambda_2)$ enables all the necessary criteria to be satisfied and connects r_2, λ_2 with the least squares sum of eq 12.

To construct $P_n(r, \lambda_n)$, $n > 2$, one must obtain $P_m(r, \lambda_m)$ for all $m < n$. The minimization equations are readily coded by writing the binary equivalents of all the integers I , $0 \leq I < 2^{n-1}$. For example, for $n = 4$, one considers 000, 001, 010, 011, 100, 101, 110, 111. The bit configurations then code for all of the equations involving $P_4(r, \lambda_4)$. In numerical order, 000, 001, 010, ..., one has

$$(\partial\{G - 0\}/\partial r)_{r=r_4} - (\partial\{G - P_4(r, \lambda_4)\}/\partial r)_{r=r_4} = 0 \quad (13a)$$

$$(\partial\{G - P_1(r, \lambda_1)\}/\partial r)_{r=r_4} - (\partial\{G - P_1(r, \lambda_1) - P_4(r, \lambda_4)\}/\partial r)_{r=r_4} = 0 \quad (13b)$$

$$(\partial\{G - P_2(r, \lambda_2)\}/\partial r)_{r=r_4} - (\partial\{G - P_2(r, \lambda_2) - P_4(r, \lambda_4)\}/\partial r)_{r=r_4} = 0 \quad (13c)$$

⋮

$$(\partial\{G - P_1(r, \lambda_1) - P_2(r, \lambda_2) - P_3(r, \lambda_3)\}/\partial r)_{r=r_4} - (\partial\{G - P_1(r, \lambda_1) - P_2(r, \lambda_2) - P_3(r, \lambda_3) - P_4(r, \lambda_4)\}/\partial r)_{r=r_4} = 0 \quad (13h)$$

There are practical limitations, of course, as the number of minimization and positive-definite conditions ($\{G - P_1(r, \lambda_1) - P_4(r, \lambda_4)\}$, $\{G - P_2(r, \lambda_2) - P_4(r, \lambda_4)\}$, ... ≥ 0) increases exponentially with n . For instance, if one considered all the constraints on $P_{14}(r, \lambda_{14})$, one would reckon with $2^{14-1} = 8192$ minimization terms alone. We have examined various truncation effects, comparing results for foams and other fluid models. When applying the indirect methods, we have found that the

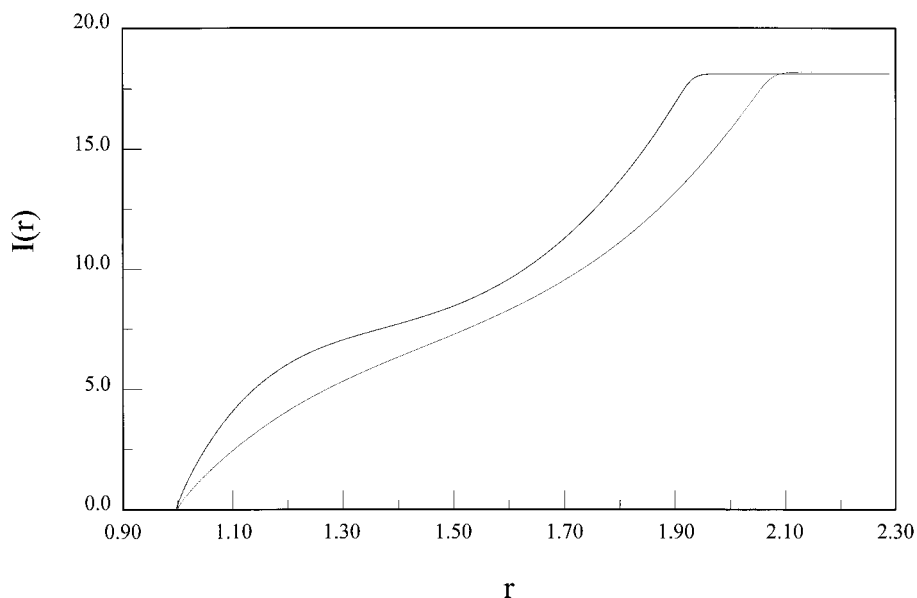


Figure 4. $I(r)$ for HS systems. Results derive from section II techniques and eq 15 analysis. Data pertain to the HS systems of Figure 1 with the thinner line allied with system "a".

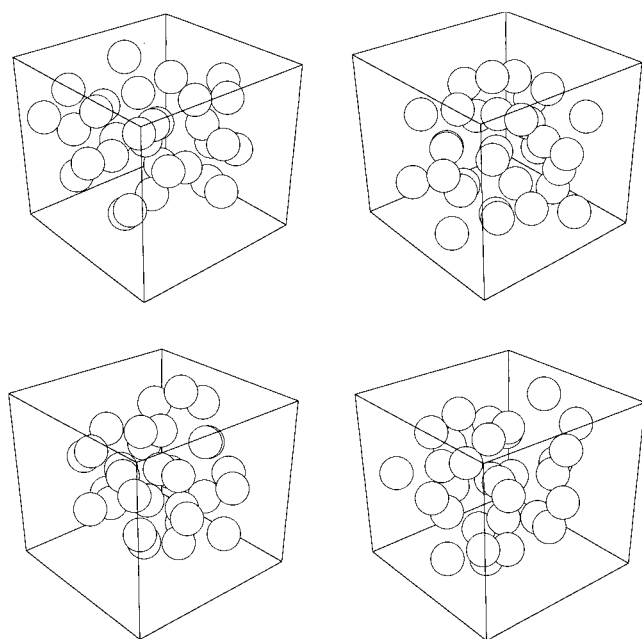


Figure 5. Atom cluster cartoons. The r values have been weighted by the best fit $P_n(r, \lambda_n)$; the x, y, z coordinates have been chosen randomly, subject to excluded volume effects. All cartoons pertain to highly probable configurations of system "a" of Figure 1.

eq 12 and 13-type constraints imposed by nearest and next-nearest neighborships ($n - 1, n - 2$) for $n > 3$ to yield satisfactory results. These constraints greatly narrow the range of allowed λ_n, r_n , making reasonable demands on processing time.

Figure 1 offers comparisons between results obtained for HS fluids using Mazur's theory⁶ and via the indirect method (black and white squares, respectively). Illustrated are the maximum values of the $P_n(r, \lambda_n)$ for $n = 1, 2, \dots, 30$, as a function of r_n , the radial position at which each neighborhood maximum is located. For simplicity, the diameters of the fluid particles have been set equal to unity and the results for two packing conditions are shown. In our experience, striking agreement is found for

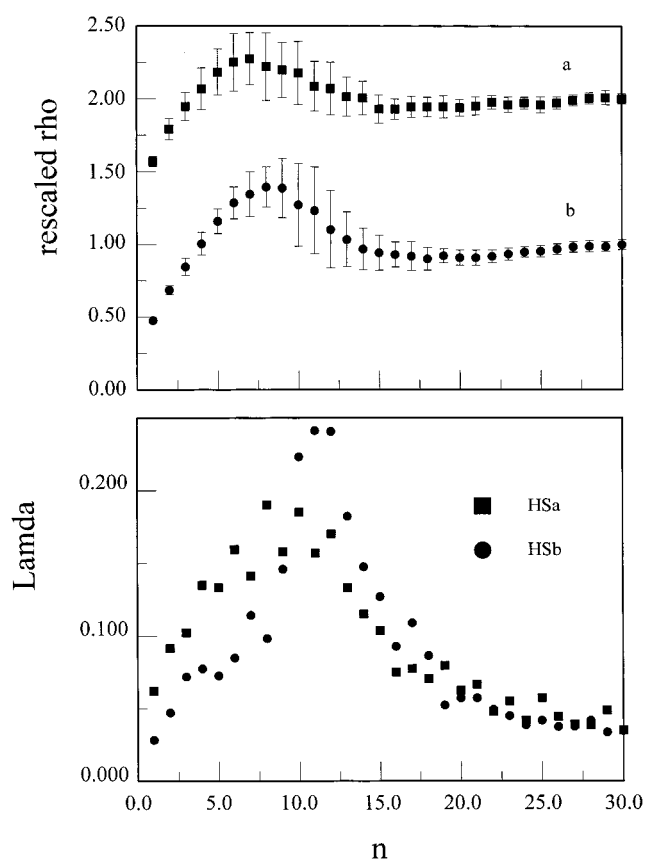


Figure 6. $\langle \rho_n \rangle \pm \sigma_n$ and $\Lambda_n = \sigma_n / \rho_n$ versus n . Data pertain to Figure 1 systems and were computed via the indirect method. A unity offset has been applied to system "a" data in the upper panel.

all of the HS neighborships except the first, irrespective of sample density. Even then, theory and the indirect method are in close agreement regarding the value of r_1 . Figure 2 shows several distributions obtained from theory and the indirect method. While the disagreement for $n = 1$ is unfortunate, such is not found in foam modeling experiments. More important

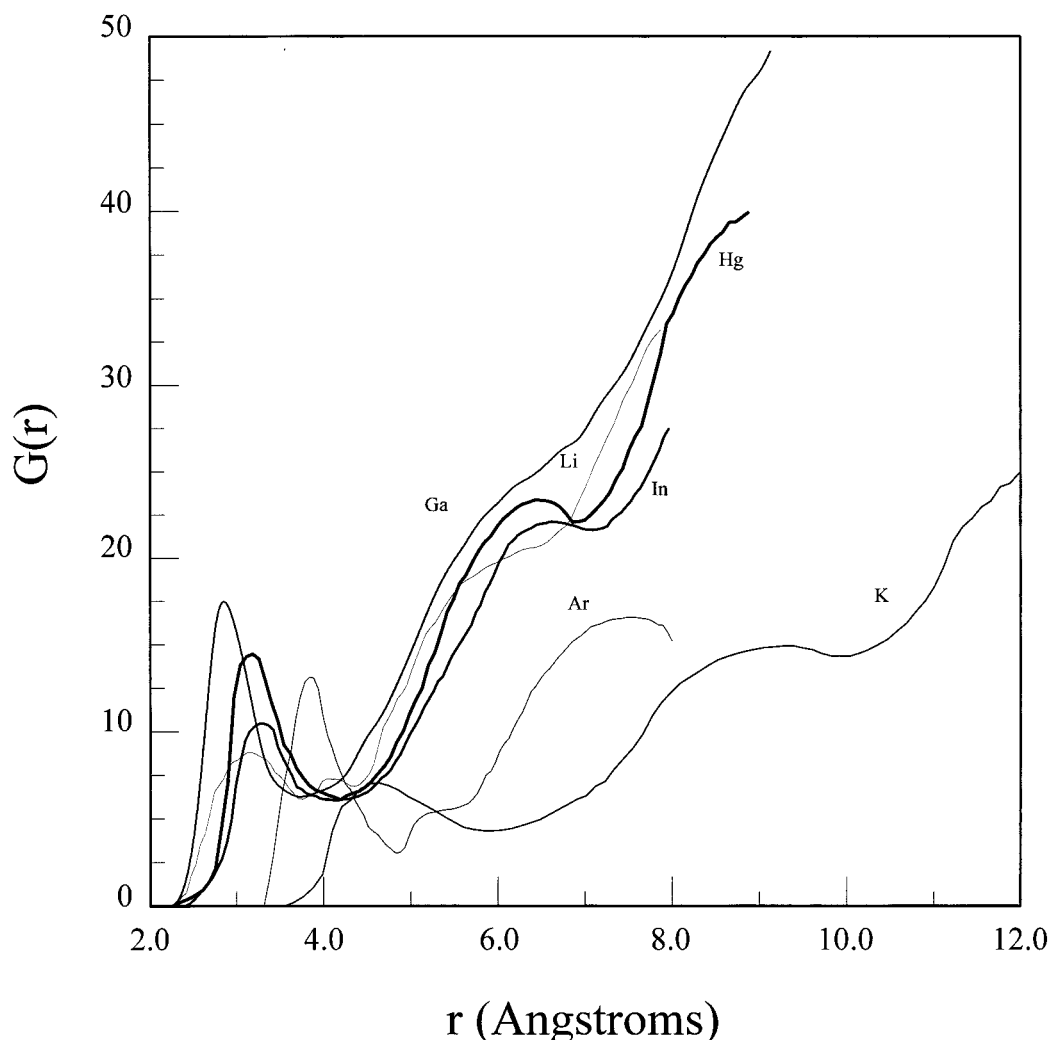


Figure 7. $G(r)$ for several monatomic liquids. Data derive from ref 11. System temperatures are noted in text. The plots can be distinguished on the basis of line thickness/atomic number: the thinnest line has been reserved for Li ($Z = 3$) and the thickest for Hg ($Z = 80$).

(in our opinion) is the close agreement between two very different approaches throughout the peaks and valleys of $G(r)$.

Results such as above and with foam models encourage applications to real liquids. To assist in the task, a few additional quantities are illustrated for HS samples.

Figure 3 depicts contour plots based on the neighborhood overlap. A variation of these was used in the previous work⁸ whereby the plots are based on the following integral:

$$O_{n,n'} = \int dr P_n(r, \lambda_n) P_{n'}(r, \lambda_{n'}) \quad (14)$$

The Figure 3 data pertain to the first 30 neighborships, with the upper panels relevant to the Figure 1 systems. Thus, the quantities $n, n' = 1 \dots 30$ lie along the ordinate and abscissa, with 1,1 marking the lower left-hand corner of each square. The lower panels feature the neighborhood analysis for two crystal morphologies: face-center-cubic (FCC) and body-center-cubic (BCC). Several things are evident. For example, the overlap structure allied with two distinct solvent shells is indicated in the upper panels, with the "void region" between shells becoming more pronounced with increased sample density. One also finds the second shell overlap to dilate as the fluid density is decreased. In comparing the upper and lower panels, one notes the overlap to be markedly different for fluids and crystals. For the latter, the overlap manifests as discrete blocks whose widths depend on the lattice symmetry.

Figure 4 addresses the neighborhood overlap in a different manner via the function $I(r)$

$$I(r) = \sum_{n \leq n'} \int_0^r dr' P_n(r', \lambda_n) P_{n'}(r', \lambda_{n'}) / G(r') \quad (15)$$

$I(r)$ can be viewed as a gauge of the neighborhood overlap density away from the reference particle. For the HS systems illustrated, $I(r)$ increases sharply with sample density near r equal to the particle diameter. Likewise, the slope of $I(r)$ near r between one and two particle diameters increases as the solvation shells become more distinct.

Figure 5 illustrates cartoons of 1 + 30 atoms based on the reference particle and its first 30 neighborships. Here, sets of radial distance values $\{r_{(n)}\}$ —not necessarily associated with the neighborship maxima—were chosen as random variables weighted by the $P_n(r, \lambda_n)$, with the condition that $0 < r_{(1)} \leq r_{(2)} \leq r_{(3)} \dots \leq r_{(30)}$. Upon identifying an allowable $\{r_{(n)}\}$ set, a 3D coordinate set $\{x_{(n)}y_{(n)}z_{(n)}\}$ was constructed quasi-randomly, with the constraints that for each n , $x_{(n)}^2 + y_{(n)}^2 + z_{(n)}^2 = r_{(n)}^2$, and that all interparticle separations exceeded the minimum specified by $G(r)$. One must be wary when converting 1D information into 3D. Moreover, the cartoons do not suggest the atoms of a fluid are at fixed sites. Nonetheless, Figure 5 offers reasonable "snapshots" of local structure. These appeal on an intuitive level, emulating the effects of multiple particle correlations. At a given

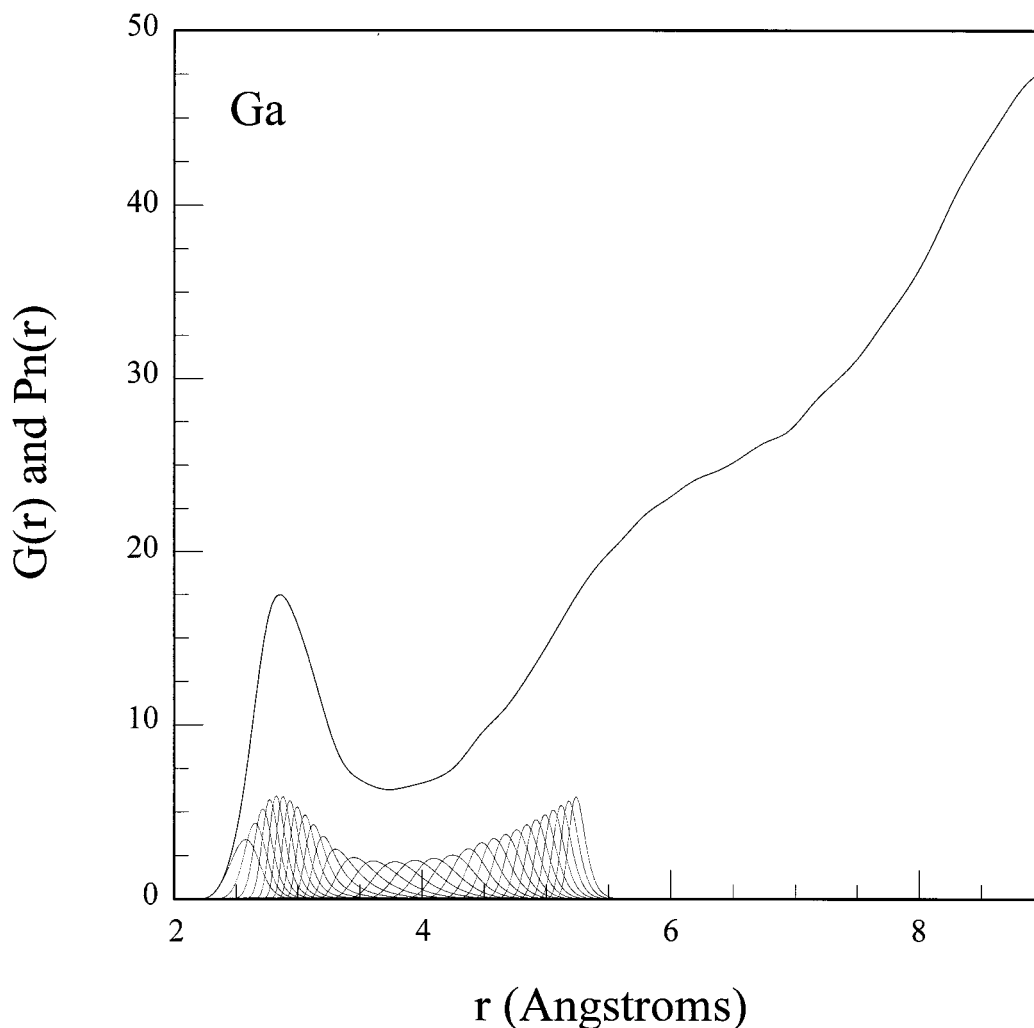


Figure 8. $G(r)$ and neighbor-ship distributions for liquid Ga, $\Delta T \approx -12$ K. Data derive from ref 12 and application of section II techniques.

instant, a fluid may be envisaged by a large, interwoven collection of these snapshots.

Figure 6 builds upon Figure 5. If one imagines a sphere about the reference particle with radius $r_{(n)}$, the centers of $1 + n$ particles are contained within the sphere or on its surface. The density ρ_n allied with the sphere is $(1 + n)/(4/3)\pi r_{(n)}^3$. Obviously, there are myriad allowed sets of $r_{(n)}, \rho_n$. The upper panel of Figure 6 thus shows a weighted average $\langle \rho_n \rangle \pm 1$ standard deviation σ_n as a function of n . These plots were constructed on the basis of many cartoons such as in Figure 5. In constructing Figure 6, the data have been rescaled by dividing $\langle \rho_n \rangle, \sigma_n$ by the density allied with $n = 30$; a unity offset has been imposed in one case for clarity. The lower panel contains a plot of the ratio $\Lambda_n = \sigma_n / \langle \rho_n \rangle$ versus n .

For a fluid, the atom arrangement is intermediate between ordered and random. Figure 6 speaks to this by showing “structure” in the $\langle \rho_n \rangle$ functionality (upper panel) to extend to ca. 15 neighborships: $\langle \rho_n \rangle$ rises and falls for $1 < n < 15$ and is “flat” for $n > 15$. The latter number exceeds one solvent shell about the reference particle, with the precise value depending ever so slightly on the sample density. Interestingly, the σ_n are greatest in the region of $n = 8-12$, depending on the sample density. This corresponds to the boundary region for the two solvent shells. Additional effects are expressed via Λ_n (lower panel) which shows the fluctuation magnitudes to increase with the fluid density. One notes also how the peak of Λ_n

shifts to higher n values and sharpens with increased sample density.

Figures 3–6 elaborate on the structure vision contained in $G(r)$. The same elaboration can be acquired via simulations such as MC and MD. Yet the path chosen here is an indirect method making no utilization of interaction potentials. In the next section, the analogous images are presented for several real liquids. These convey the essentials of neighbor-ship distributions and offer structure comparisons among diverse systems.

III. Neighbor-ship Data for Several Monatomic Liquids

The literature is rich with structure data for the elements. While results from different labs show discrepancies, it would appear that the essential diffraction and atom distribution traits for the Table 1 systems have been well established. We have based the analyses reported here on such traits, as compiled by Gingrich and Wyckoff for liquids and crystals, respectively.^{11,12} We note the results to change little when incorporating data reported in other places.¹³ Thus, for all of the systems, $G(r)$ data were digitized and interpolated as in previous work.⁸ The end results were faithful, near-continuous representations of the distribution curves. The section II methods were then applied to yield $P_n(r, \lambda_n)$ for $n \leq 30$. The n limit was chosen to focus attention on the first two solvent shells.

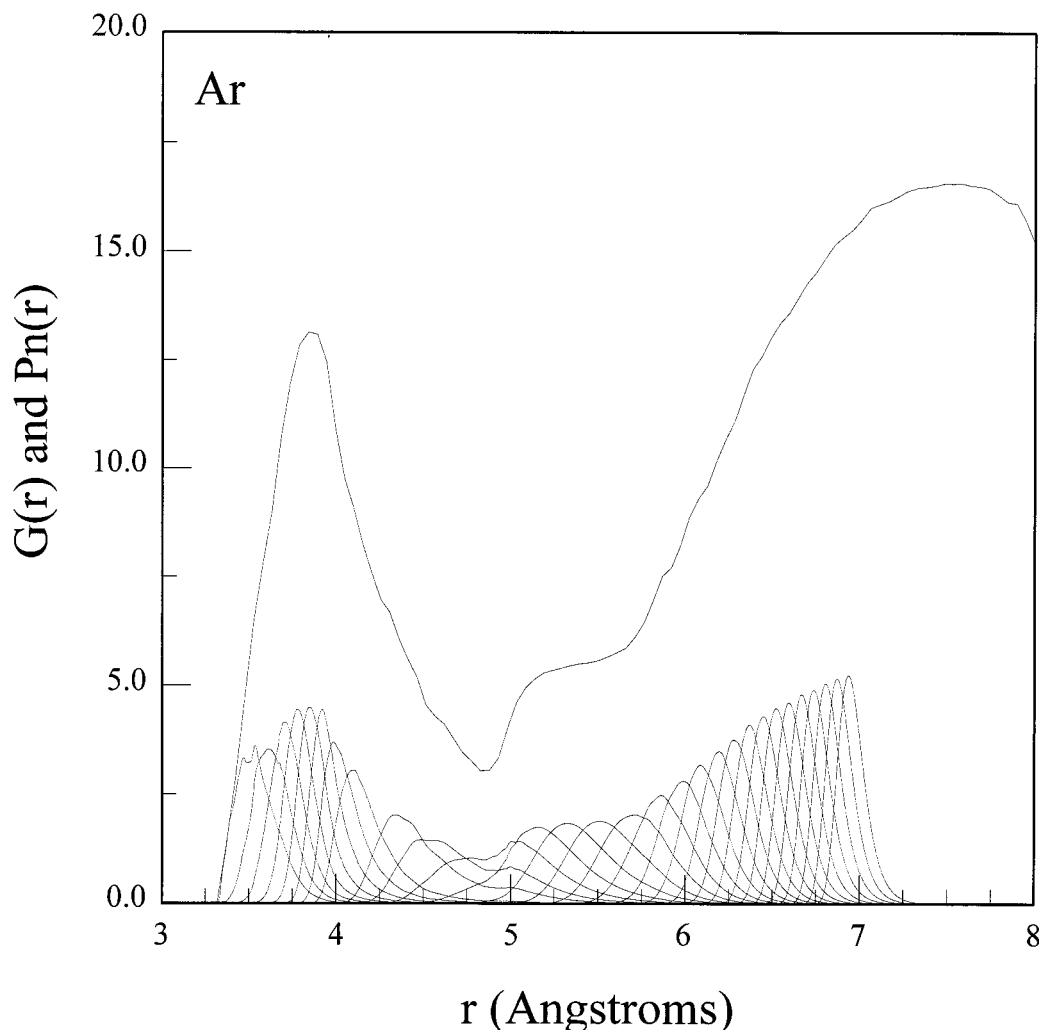


Figure 9. $G(r)$ and neighborhood distributions for liquid Ar, $\Delta T \approx 0.5$. Data derive from ref 11 and application of section II techniques.

Representative results are illustrated in Figures 7–9. Shown are $G(r)$ (Figure 7) for the Table 1 species at the following temperatures: Ar ($\Delta T \approx 0.5$ K), Ga (-12 K), Hg ($+60$ K), In ($+5$ K), K ($+8$ K), and Li ($+14$ K). The values in parentheses refer to the degrees above or below the freezing point. The distribution plots can be distinguished on the basis of line thickness/atomic number: the thinnest line has been reserved for Li ($Z = 3$) and the thickest for Hg ($Z = 80$). Figures 8 and 9 depict $G(r)$ and best-fit $P_n(r, \lambda_n)$ for liquid Ga and Ar. In all cases, the $G(r)$ features are broad and diffuse with only a few peaks at best. The computed neighborhoods of Figures 8 and 9 manifest different heights, widths, and tails; all are observed to be monomodal except for Ar near $r = 3$ and $r = 5$ Å. Other properties can be cited; however, to draw systematic comparisons is not so clear cut by the distribution curves alone. This is where the tools of Figures 3–6 assist.

Figure 10 illustrates overlap plots for the six elements, with all panels concerning the first 30 neighborhoods. Figure 11 illustrates the analogous plots based on the crystal structures. Where more than lattice type has been identified, such as for Ga and Hg,¹² only the most prominent one has been selected for illustration.

Figure 12 contains $I(r)$ for the different systems. In preparing this graph, r has been made dimensionless by dividing it by the minimum separation between the reference atom and its nearest neighbor. As with Figure 7, the Figure 11 plots are

distinguishable on the basis of line thickness/atomic number. A few observations are as follows. $I(r)$ for Ar and Ga near $r = 1.50$ exceeds that of the other systems; this region corresponds to the middle of the first solvent shell. Sigmoidal features are observed in all six cases with the $I(r)$ functionality for In and Li nearly coincident. The slope of $I(r)$ for Ar and Ga near $r = 1$ exceeds that demonstrated by the other systems.

Atom cluster cartoons appear in Figure 13, each suggesting a random packing nature subject to excluded volume effects. The Ar cluster appears less ramified than the other systems. In turn, the excluded and free volume are distributed most uniformly for Ar.

In Figures 14 and 15 are illustrated $\langle \rho_n \rangle \pm \sigma_n$ and Λ_n with both similarities and differences to be noted. For example, the “structure” in $\langle \rho_n \rangle$ extends to ca. 19 neighborhoods in Ga while only 12–15 for the other systems. The n values for which $\langle \rho_n \rangle$ demonstrates a maximum are roughly the same for all of the systems. In Figure 15, the n values for which Λ_n demonstrates a maximum are as high as 15 for Ga while only 8 for Li; the Λ_n functionality is sharpest for Ga in the mid-abscissa region. Also, for Hg, K, In, Li, and Ga, Λ_n decreases markedly over the range $n = 1$ –4. This behavior is suppressed for Ar and the HS systems.

Structure data are available over a range of temperature.^{11–13} Figures 16–19 give attention to this by showing results for Ar under four conditions: $T = 84, 92, 127$, and 144 K ($\Delta T \approx +$

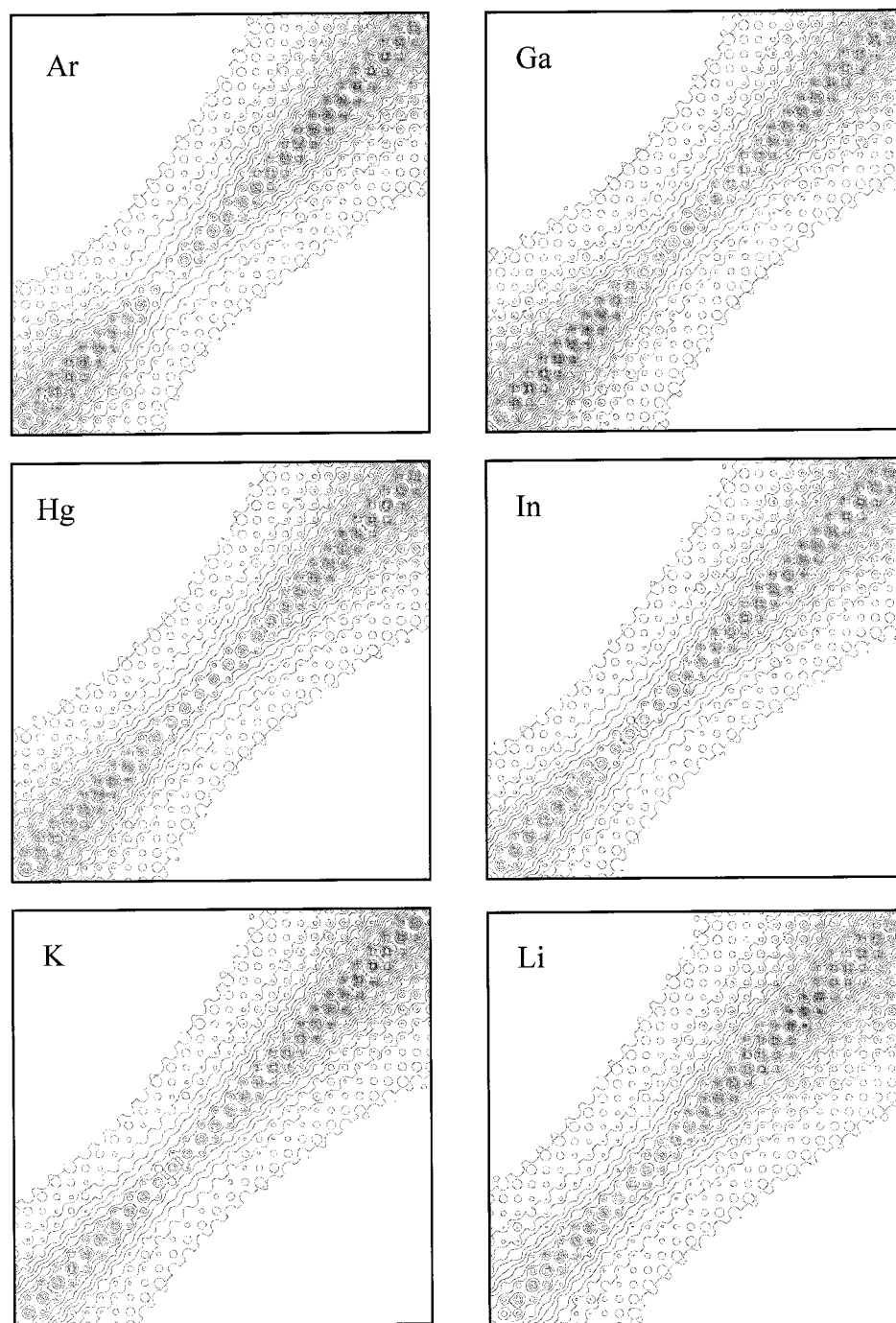


Figure 10. Contour plots derived from neighborhood overlap; $n, n' = 1-30$. Data pertain to systems illustrated in Figure 7. Identical scaling parameters have been used in all six cases.

0.5, 8, 43, and 60 K). The overlap plots in Figure 16 show the void between the solvent shells to become accentuated at lower temperatures. The first shell contour narrows and becomes less pronounced with increasing temperature. In all cases, the contour structure differs markedly from the FCC crystalline case of Figure 11. In Figure 17, one finds $I(r)$ to diminish in magnitude and slope for $T = 84-127$ K. Note the $I(r)$ functionality to be markedly different at $T = 144$ K, compared with the lower temperature cases. In particular, the sigmoidal characteristics are nearly absent at the highest of the liquid temperatures.

Figure 18 depicts atom cluster snapshots for Ar at the same four temperatures. These show the packing uniformity to decrease with increasing temperature. Such is reiterated in

Figures 19 and 20 where the maximum in $\langle \rho_n \rangle$ extends to higher n values with decreasing temperature. The deviations in $\langle \rho_n \rangle$ from the terminal value at 84 K exceed those at 144 K by more than a factor of 2. In Figure 20, Λ_n demonstrates a maximum value at $n = 12$ for $T = 84$ K; at $n = 5$ for $T = 144$ K.

IV. Discussion

For a fluid, $G(r)$ quantifies the number of first- and second-shell neighbors, the pair correlation length, the atomic size, and sample density.¹ More detailed information at the molecular level, however, is severely limited.¹⁴ The aim in section III was to extend the picture offered by $G(r)$. The results are interesting

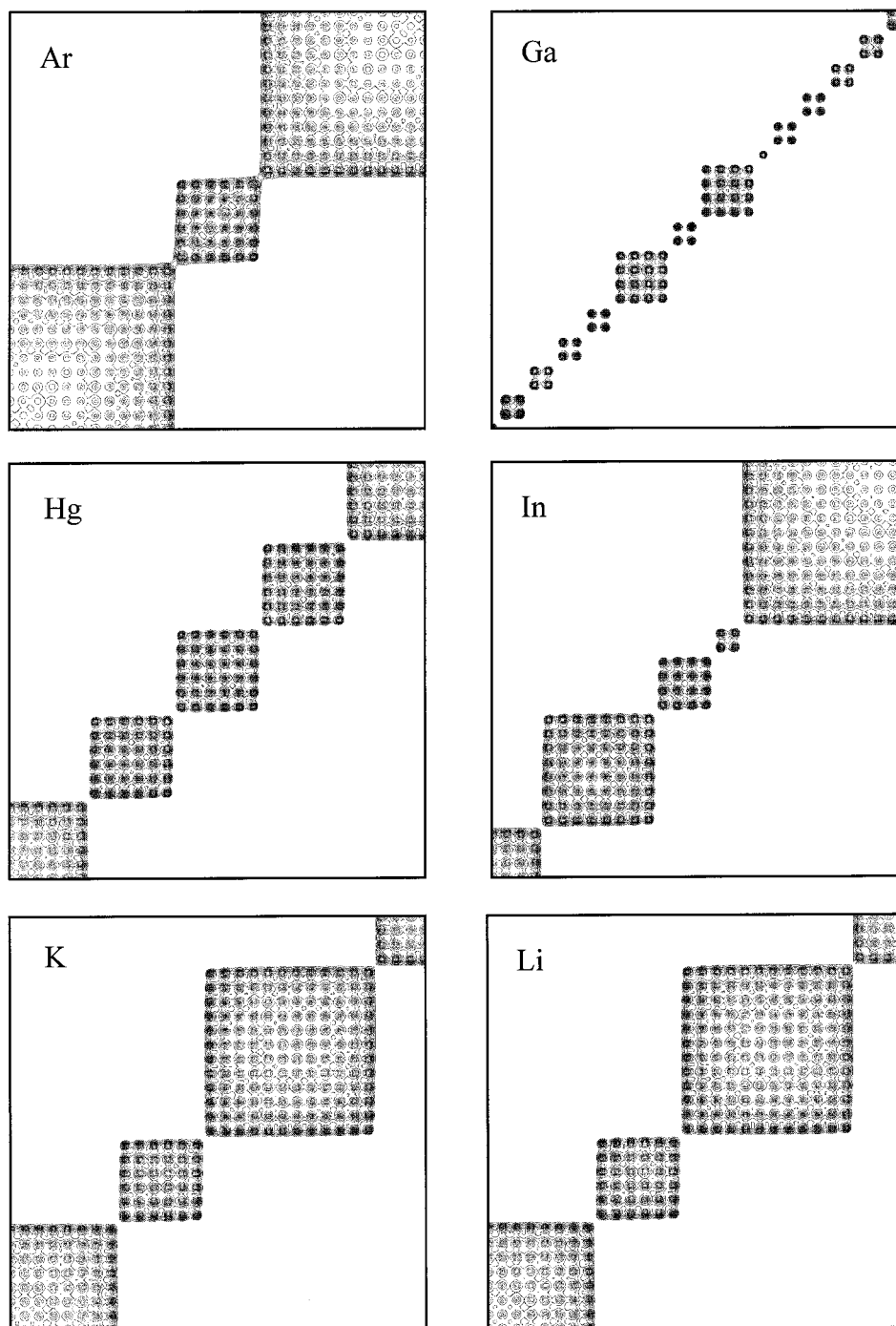


Figure 11. Neighborhood overlap for crystals; $n, n' = 1-30$. The panels follow from data contained in ref 12: Ar, face-center-cubic with 4 atoms/unit cell; Ga (α form), orthorhombic with 8 atoms/unit cell; Hg (α form), rhombohedral with 1 atom/unit cell; In, tetragonal with 2 atoms/unit cell, K and Li, body-center-cubic with 2 atoms/unit cell.

because they propose neighborhood distributions for real systems. In doing so, they reinforce important themes about liquids and suggest structure–function relationships.

There are at least two reinforced themes, the first being a similarity of structure among diverse materials. This idea has been realized many times in MC and MD simulations.^{15,16} One grasps this via the cluster snapshots such as in Figure 13, the gross structure differences for Ar, Ga, etc. prove only minor. This theme is crucial to liquid structure and dynamics. Among other things, it accounts for the similarity of $G(r)$ for chemically different systems.^{17,18} Indeed, the scaling of $I(r)$ proves nearly identical for In and Li.

Figure 16 indicates the structure changes with temperature to be subtle. Yet these can be highlighted by the quantities $\langle \rho_n \rangle$, Λ_n , and $I(r)$. Importantly, one becomes aware how the solvation shell concept becomes diminished with increasing temperature. Note how the fluctuations gauged by Λ_n increase with increasing temperature. Further, the peak in Λ_n inches closer to the reference particle as temperature is increased. Apparently, the overlap sensitivity to temperature is most marked in the first few neighborhoods; the morphology changes with temperature are thus unequally weighted among different solvent shells. This trait seems especially apparent in $I(r)$ as a function of temperature. For Ar at $T = 144$ K, $I(r)$ gives only

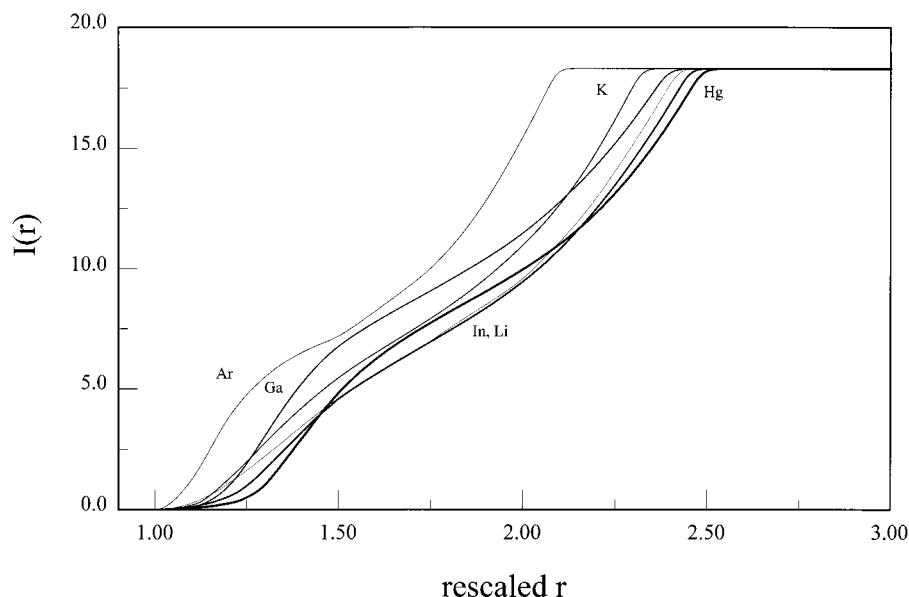


Figure 12. $I(r)$ for different liquids. The radial distance r has been rescaled by dividing it by the minimum separation distance between the reference particle and its nearest neighbor. As in Figure 7, the line thicknesses increase with increasing system atomic number. Data pertain to Figure 7 materials.

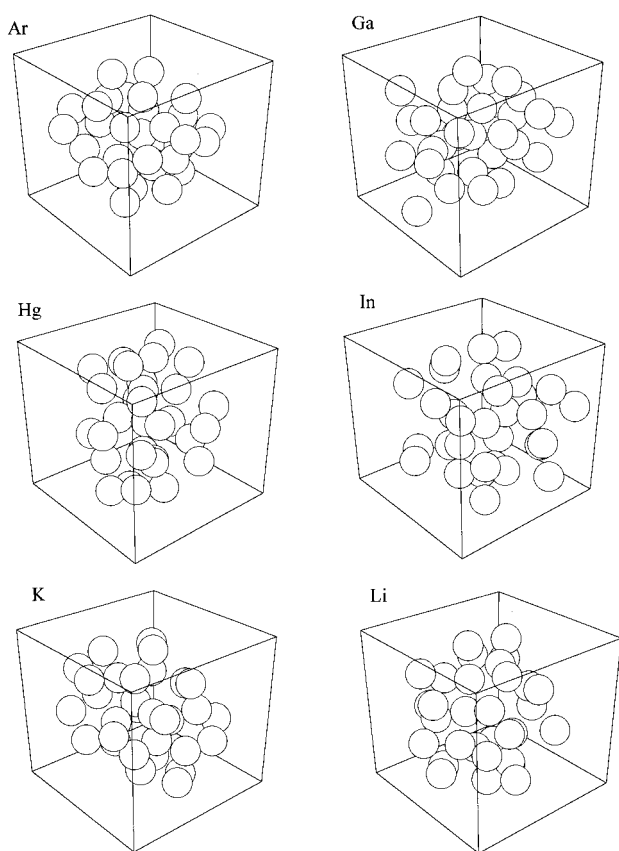


Figure 13. Atom cluster cartoons. All cartoons depict highly probable configurations of Figure 7 materials.

trace indication of the first solvent shell, in sharp contrast to the lower temperature results.

A second theme is the marked differences between liquids and their corresponding crystals. Structural disparities appear to be the “rule” and we have encountered no exceptions to date. Over the years, such a view has acquired currency in several models of liquid structure.¹⁹ For our part, contour plots such as

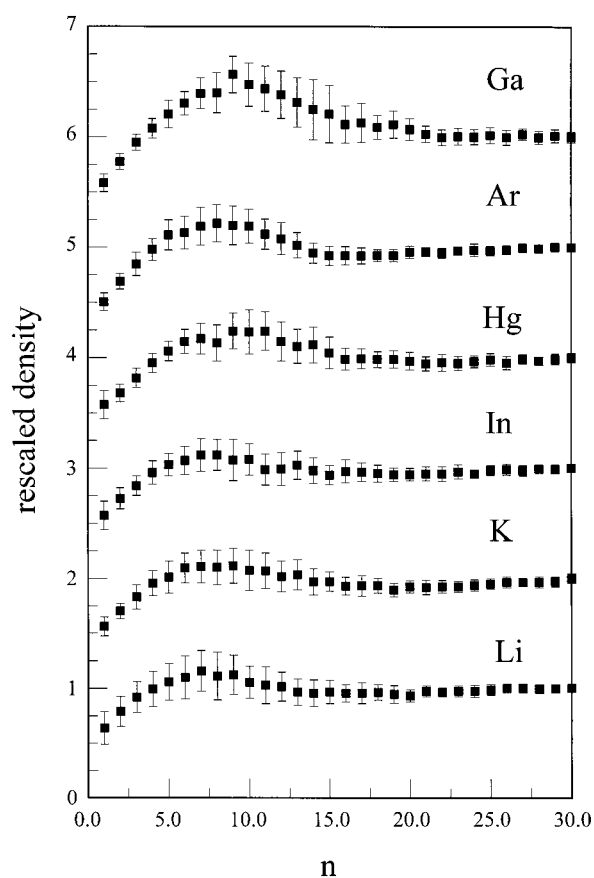


Figure 14. $\langle \rho_n \rangle \pm \sigma_n$. Data pertain to Figure 7 materials with offsets imposed for clarity.

in Figures 8, 9, and 16 offer additional tools for comparing liquid and crystal structure. The plots are especially useful for their reliance on dimensionless variables n , n' . This enables comparisons across a spectrum of materials in ways unafforded by $G(r)$ alone.

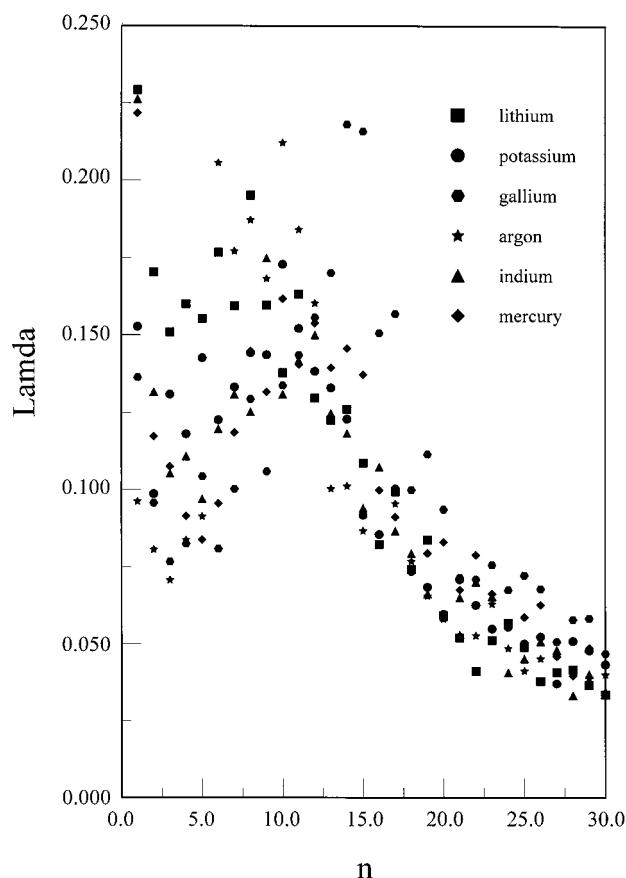


Figure 15. $\Lambda_n = \sigma_n / \rho_n$ versus n . Data pertain to materials of Figure 7.

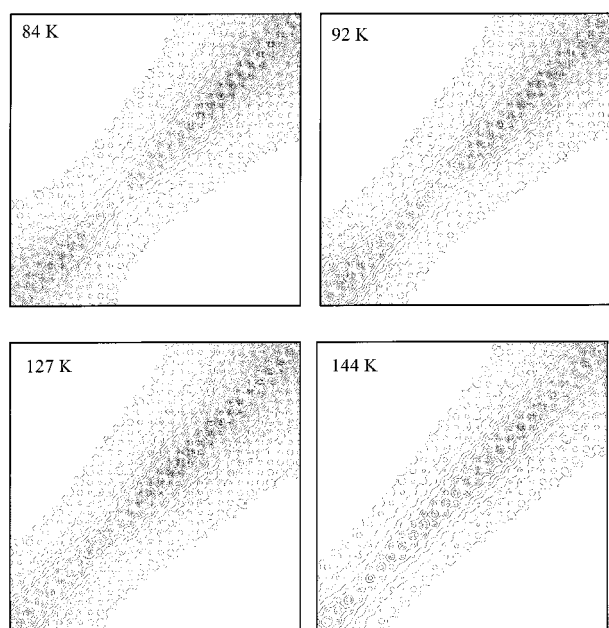


Figure 16. Neighborhood overlap for liquid Ar. Identical scaling parameters have been used in all cases. Inset values refer to liquid temperature at which original diffraction data were recorded.

The contour plots show the similarities between liquids and crystals to be subtle in degree. Yet several features are interesting, especially in connection with possible scenarios for freezing and melting. For example, the extent of overlap in the

first shell for liquid K and Li is closer to that observed in FCC states than in BCC states. Solid K and Li both evince BCC structures. This suggests the possibility of FCC intermediates during the freezing of liquid K and Li. The situation appears different for Ar. For this material near the freezing point, the extent of first-shell overlap closely adheres to that of an FCC crystal. Crystalline Ar has an FCC structure thus suggesting that liquid Ar freezes with no extraneous intermediates (e.g., BCC) along the way. For liquid In, the extent of overlap in the first shell matches that of the second shell of the crystal. This suggests that during freezing, the second crystalline shell may be born prior to the innermost shell.

In connecting structure and function, a neighborhood view may be particularly important for Ga. For this liquid, the gross features of $O_{n,n'}$ and $I(r)$ resemble those of the other systems. Yet some distinguishing characteristics are also apparent. The overlap within the first solvent shell of liquid Ga extends to ca. 15 neighborships; this exceeds the overlap observed for the other materials. Also, the neighborhood overlap for crystalline Ga is very fragmented, at least for the α -form. By contrast, the liquid manifests an $O_{n,n'}$ functionality which is much more continuous.

There are other quirks which emerge from the Ga results. The extent of structure in the $\langle \rho_n \rangle$ functionality appeared greatest for this element and its Λ_n functionality proved sharpest. Structure in $\langle \rho_n \rangle$ stems from the changes in the excluded/free volume ratio with distance from the reference atom; Λ_n reflects the density fluctuations allied with each neighborhood. Overall, these quantities indicate an unusually extended structure in liquid Ga, compared with other systems. Moreover, the exchange of atoms between solvent shells occurs most prevalently well away from the reference site, specifically involving the 14th and 15th neighborships.

The foregoing may be important because of Ga's nonequilibrium phases and resistance to crystallization.^{20,21} Moreover, the temperature difference $\Delta T \approx 2390$ K between the freezing and boiling points is the largest of all the elements, not just those discussed here. Such properties bespeak an unusual stability for liquid Ga. Explaining supercooling behavior, multiple phases, and differences between melting and boiling points is no easy task. Yet the peculiar structure and function of condensed Ga appear to hinge on the neighborhood distribution details.

Liquid structure is determined largely by repulsive interactions between atoms. This fact underlies the structure similarities among different systems and enables many approximations of the interatomic potentials. Introduced in the foam studies and applied further in this paper are techniques which sidestep the potential specifics. As such, the techniques can be exercised in much the same spirit as in crystallographic analysis. In the latter, solid structures can be "solved" by indirect methods without precise knowledge of the atomic scale interactions. The results instead furnish insight into and questions about these interactions.

An expanded view of $G(r)$ does much the same for liquids. Concerning questions raised, note that only the systems incapable of covalent interactions, Ar and HS, demonstrated ascending behavior of Λ_n at low n values. The other samples evinced descending behavior of Λ_n near $n = 1-4$. Such results are interesting. The question is raised whether nearest neighbors impose a local organization which is fundamentally different for covalent liquids, compared with noble gas and HS systems. For Ga, Hg, Li, K, and In, the data indicated significant variability in the placement of 3-4 atoms nearest the reference

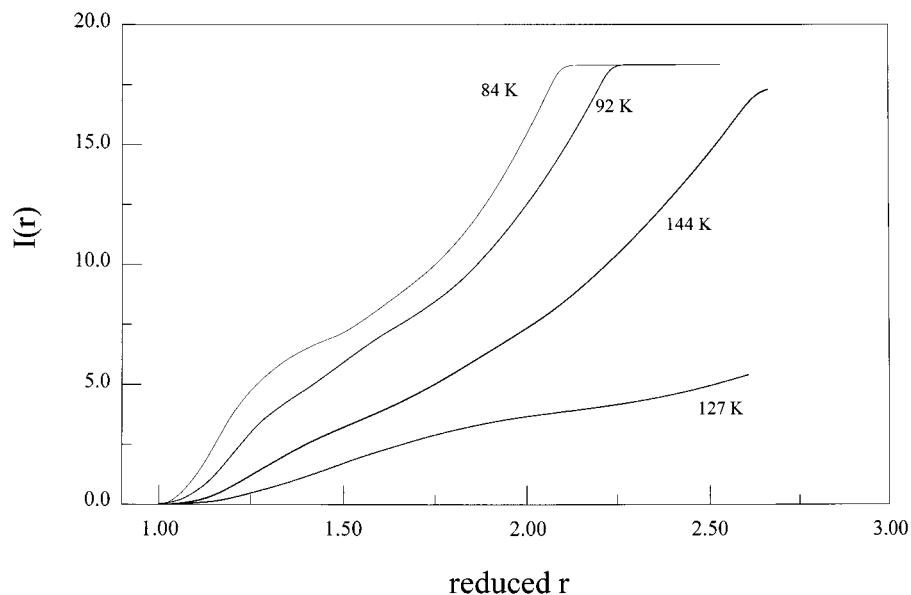


Figure 17. $I(r)$ for liquid Ar. The radial distance has been rescaled as in Figure 12. The line thicknesses increase with increasing temperature. Data pertain to Figure 16 systems.

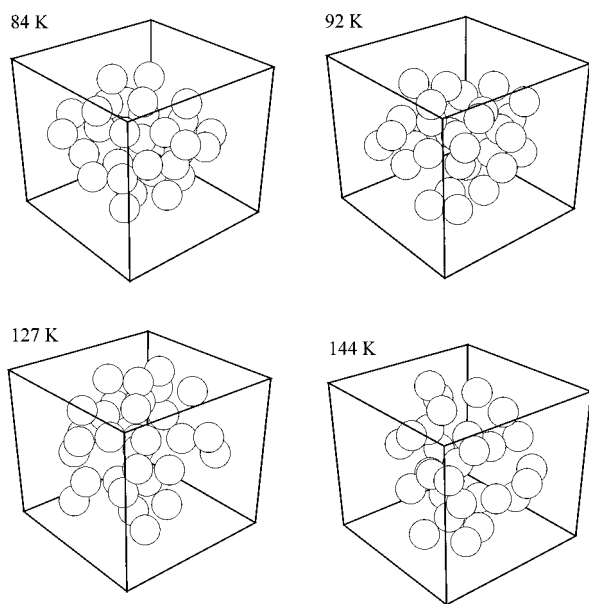


Figure 18. Atom cluster cartoons for liquid Ar. The cartoons depict highly probable configurations of the Figure 16 systems.

site. This suggests a greater complexity for the first solvent shell than is apparent in $G(r)$ by itself. Chemical structure theory sharply distinguishes materials such as Ga and Ar. The results here question whether this theory and its central idea of valence can assist in our understanding of liquid structure.

V. Summary and Closing

Liquid structure can be described using best-fit neighborhood distribution functions and several auxiliary quantities. While the description cannot be corroborated unambiguously by lab experiment, the techniques which lead to it are simple to apply and lend insight into liquid structure and function. The techniques are not intended to replace MC and MD simulations.

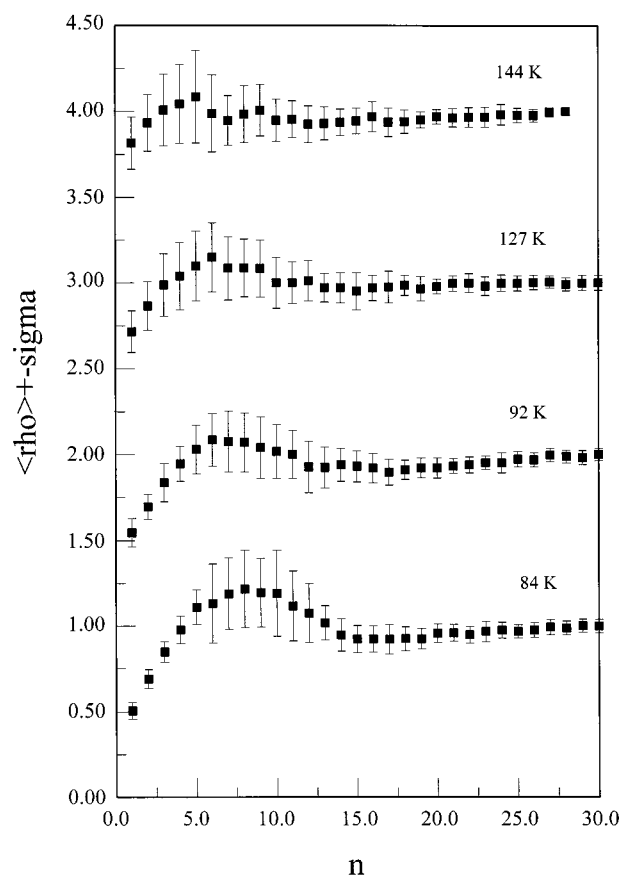


Figure 19. $\langle \rho_n \rangle \pm \sigma_n$. Data pertain to Figure 16 systems with offsets imposed for clarity.

Rather they should find greatest utility when knowledge of interaction potentials is lacking.

The section II techniques are not limited to monatomics. At present we are investigating the molecular systems N_2 , P_4 , S_8 , and the halogens. We are further working to connect $\langle \rho_n \rangle$ and σ_n with thermodynamic quantities.

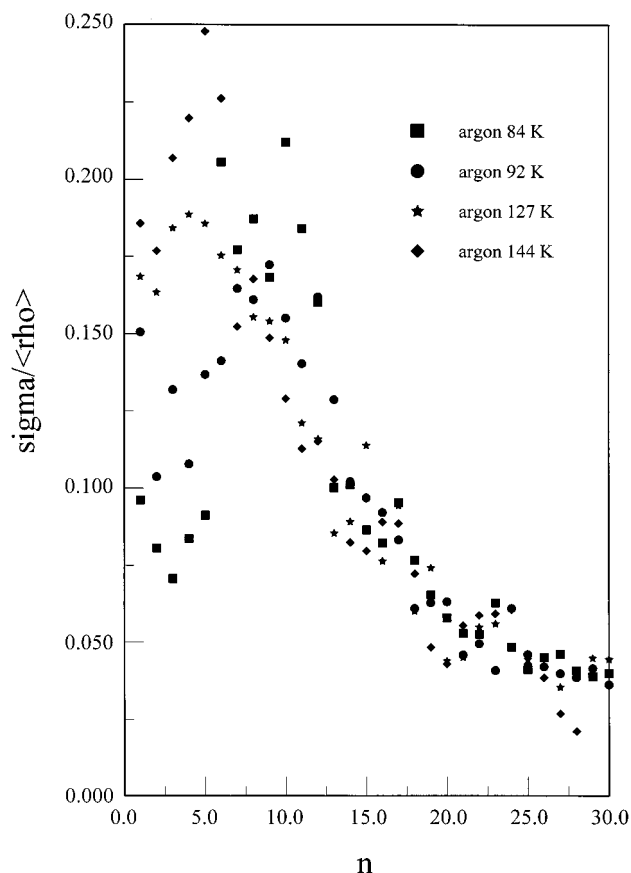


Figure 20. $\Lambda_n = \sigma_n / \rho_n$ versus n . Data pertain to systems of Figure 16.

Acknowledgment. The authors appreciate helpful discussions with Professor Stephen Pavkovic about crystal structure and X-ray diffraction data.

References and Notes

- (1) Barker, J. A.; Henderson, D. *Rev. Mod. Phys.* **1976**, *48*, 587. Egelstaff, P. A. *An Introduction to the Liquid State*; Academic: New York, 1967. Hansen, J. P.; McDonald, I. R. *Theory of Simple Liquids*; Academic: London, 1976.
- (2) Hertz, P. *Math. Ann.* **1909**, *67*, 387. See also: Reiss, H.; Frisch, H. L.; Lebowitz, J. L. *J. Chem. Phys.* **1959**, *31*, 369.
- (3) Torquato, S.; Lu, B.; Rubinstein, J. R. *Phys. Rev. A* **1990**, *41*, 2059. Torquato, S.; Lee, S. B. *Physica A* **1990**, *16*, 361.
- (4) MacDonald, J. R. *J. Phys. Chem.* **1992**, *96*, 3861.
- (5) McGreevy, R.; Baranyai, A.; Ruff, I. *Phys. Chem. Liq.* **1986**, *16*, 47.
- (6) Mazur, S. J. *J. Chem. Phys.* **1992**, *97*, 9276.
- (7) Keyes, T. J. *J. Chem. Phys.* **1999**, *110*, 1097.
- (8) Graham, D. J.; Magdalinos, P.; Pimentel, D. *J. Phys. Chem. B* **1998**, *101*, 11211.
- (9) Graham, D. J.; Magdalinos, P.; Tosi, M. J. *J. Phys. Chem.* **1995**, *99*, 4757.
- (10) See, for example: Graham, D. J. *J. Phys. Chem.* **1991**, *95*, 993. Graham, D. J.; LaBrake, D. L. *J. Phys. Chem.* **1991**, *95*, 997. Graham, D. J.; LaBrake, D. L. *J. Phys. Chem.* **1993**, *97*, 5594. Graham, D. J.; LaBrake, D. L. *Appl. Spec.* **1993**, *47*, 625.
- (11) Gingrich, N. S. *Rev. Mod. Phys.* **1943**, *15*, 90.
- (12) Wyckoff, R. W. G. *Crystal Structures*; Wiley: New York, 1963; Vol. I.
- (13) Kruh, R. F. *Chem. Rev.* **1962**, *62*, 319. Furukawa, K. *Rep. Prog. Phys.* **1965**, *28*, 169.
- (14) Karnicky, J. F.; Pings, C. J. *Adv. Chem. Phys.* **1976**, *34*, 157. See also: Wheatley, P. J. *The Determination of Molecular Structure*; Dover: New York, 1968; Chapter 8.
- (15) Doye, J. P. K.; Wales, D. J. *Science* **1996**, *271*, 484.
- (16) Allen, M. P.; Tildesley, D. J. *Computer Simulations of Liquids*; Clarendon: Oxford, 1987.
- (17) Chen, S.-H. *Structure of Liquids in Physical Chemistry, An Advanced Treatise*; Henderson, D., Ed.; Academic: New York, 1971; Vol IIIA, Chapter 2.
- (18) Paskin, A. *Adv. Phys.* **1967**, *16*, 223.
- (19) See, for example: Bernal, J. D. *Nature (London)* **1959**, *183*, 141. Bernal, J. D. *Nature (London)* **1960**, *185*, 68. Bernal, J. D. *Proc. R. Soc. London* **1964**, *280*, 299. Morrell, W. E.; Hildebrand, J. H. *J. Chem. Phys.* **1936**, *4*, 224.
- (20) Downs, A. J. *Chemistry of Aluminum, Gallium, and Thallium*. In *Chemistry of the Group 13 Metals: Some Themes and Variations*; In *Chemistry of Aluminum, Gallium, Indium, and Thallium*; Downs, A. J., Ed.; Blackie Academic and Professional: London, 1993; Chapter 1.
- (21) Defrain, A. J. *J. Chem. Phys.* **1977**, *74*, 851.